Kirigami-inspired Thermal Regulator: Supplemental Material

Hongyi Ouyang,[1, †] Yuanqin Gu,[2, 3, †] Zhibin Gao,[1, *] Lei Hu,[1] Zhen Zhang,[1]
Jie Ren,[4] Baowen Li,[5] Jun Sun,[1] Yan Chen,[2, 3, ‡] and Xiangdong Ding[1, §]

[1]*State Key Laboratory for Mechanical Behavior of Materials, Xi'an Jiaotong University, Xi'an 710049, China*

[2]*Key Laboratory of Mechanism and Equipment Design of Ministry of Education, Tianjin University, Tianjin, 300350, China*

[3]*School of Mechanical Engineering, Tianjin University, Tianjin, 300350, China*

[4]*Center for Phononics and Thermal Energy Science, China-EU Joint Center for Nanophononics,*
Shanghai Key Laboratory of Special Artificial Microstructure Materials and Technology,
School of Physics Sciences and Engineering, Tongji University, Shanghai 200092, China

[5]*Department of Materials Science and Engineering, Department of Physics. Southern University of Science and Technology,*
Shenzhen, 518055, PR China. International Quantum Academy, Shenzhen 518048,
PR China. Paul M. Rady Department of Mechanical Engineering and Department of Physics,
University of Colorado, Boulder, Colorado 80305-0427, USA

———————

† These authors contributed equally to this work.

* E-mail: zhibin.gao@xjtu.edu.cn

‡ E-mail: yan_chen@tju.edu.cn

§ E-mail: dingxd@mail.xjtu.edu.cn

We utilized *ab initio* density functional theory (DFT) with projector-augmented wave (PAW) pseudopotentials [49,50] and the Perdew-Burke-Ernzerhof (PBE) [51] exchange-correlation functionals, as implemented in the VASP [52,53]. We set 500 eV as the electronic kinetic energy cutoff and sampled a 7 × 7 × 1 k-point grid [54]. The self-consistency iteration for the convergence criterion is below 10^{-4} eV, and all geometries were optimized by the conjugate-gradient (CG) method until none of the residual Hellmann-Feynman forces exceed 10^{-2} eV/Å. The electronic transport properties were obtained based on the DFT combined with the nonequilibrium Green's function (NEGF) [73] using Atomistix Toolkit (ATK) package [74]. At a certain bias voltage V_b, and gate voltage V_g, the drain current is calculated from the Landauer-Büttiker formula [75],

$$I(V_g, V_b) = \frac{2e}{h}\int_{-\infty}^{+\infty}\{T(E, V_g, V_b)\cdot[f_S(E-\mu_S) - f_D(E-\mu_D)]\}\mathrm{d}E, \quad (1)$$

where $T(E, V_g, V_b)$, f_S, f_D, μ_s, μ_D are the transmission coefficient, Fermi-Dirac distribution functions, and electrochemical potentials of source and drain, respectively. To build the device, the unit cell was repeated 7 times in x direction, and the unit cells on two sides were treated as semi-infinite electrodes, while the center unit was regarded as a scattering region. The cutoff energy and k-point mesh were set to 20 Hartree and 100 × 1 × 1. For the lattice thermal conductivity κ_{lat}, we used the non-equilibrium molecular dynamics (NEMD) simulations by LAMMPS [62] and the Tersoff potential of carbon-nitrogen interaction [63]. Atoms on two sides of NPG are connected to the Nosé-Hoover thermostats with 320 K and 280 K, respectively.

Here, we further discuss the element X selecting process, stability, mechanical properties, thermal transport properties, electronic transport properties, and optical properties of NPG.

The Poisson's ratio ν, the negative ratio of lateral to applied strain, of this kirigami assembly is given,

$$\nu_{xy} = -\frac{\varepsilon_x}{\varepsilon_y} = -\frac{\mathrm{d}y/y}{\mathrm{d}x/y} = -1$$

Interestingly, ν of this kirigami assembly equals -1 which means structures in both directions expand or contract simultaneously. The deformation behavior of the assembly with different ratios between *d* and *r*, is shown in Fig. S1. When the ratio increases, the strain caused by the same change of θ will decrease.

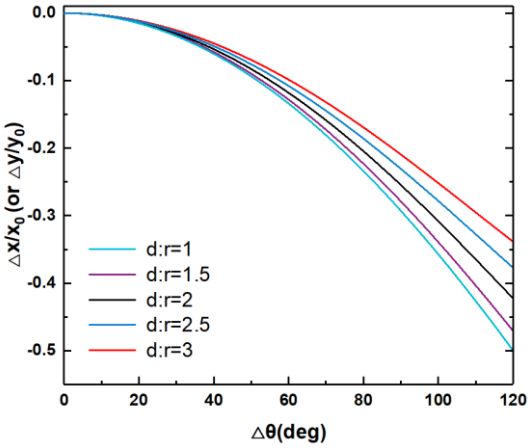

Figure S1. Strain in x or y direction dependence of θ with different ratios of d and r.

Based on the three criteria mentioned in the main text, doping element X can be decided in the following. Firstly, to obey rule (i), doping with an atomic radius significantly different from the intrinsic element will cause a large distortion of material [48]. Using the DFT calculation, we obtained the relaxed structures of porous graphene substituted by phosphorus and silicon. In the vertical direction, their structures exist with noticeable distortion, shown in Fig. S2.

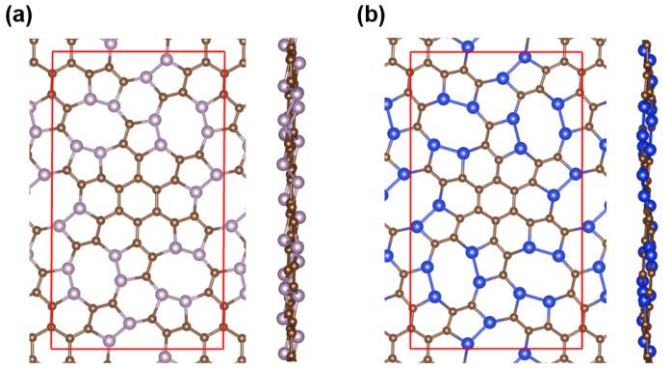

Figure S2. Vertical and side view of relaxed structures of porous graphene substituted by (a) Phosphorus and (b) Silicon.

Therefore, the selection element should belong to the same period as the carbon element. Indeed, elements of which the outermost electron is greater than five, such as Sulphur and fluorine, will lead to instability and collapsed structure, shown in Fig. S3(f-g). Thus, the *p-block* elements in the second period (B, C, N, O) are promising candidates for X in Fig.2(a). Secondly, according to the octet rule, each carbon atom in graphene has three in-plane σ bonds of sp^2 hybrid orbitals, and contributes one electron forming a π bond perpendicular to the plane. Therefore, atoms in the critical position should gain two electrons from σ bonds of sp^2 hybrid orbitals and one or zero electrons from π bond to contribute p_z orbits in the out-of-plane. That is what structure stability requires.

On the one hand, if the key position is the carbon element, the structure without saturated

hydrogen would include two bonds between modules, which disobeys rule (ii), shown in Fig. S3(a). On the other hand, if the key position is still the carbon element, the structure with saturated hydrogen would have smaller space for the folding-unfolding deformation, shown in Fig. S3(b). Besides, more bonds connecting modules will appear in structure with born elements due to less one electron compared with carbon, shown in Fig. S3(e).

Therefore, we consider nitrogen- and oxygen-substituted structures shown in Fig. S3(c-d). After the DFT optimization, we find the relaxed structure agrees commendably with the kirigami assembly. The electronic band structures are further investigated. In the equilibrium state, the oxygen-substituted metamaterial is metal. At the same time, the nitrogen-substituted is an insulator, as shown in Fig. S4. Consequently, the nitrogen element is the best winner to substitute the atom in the key position.

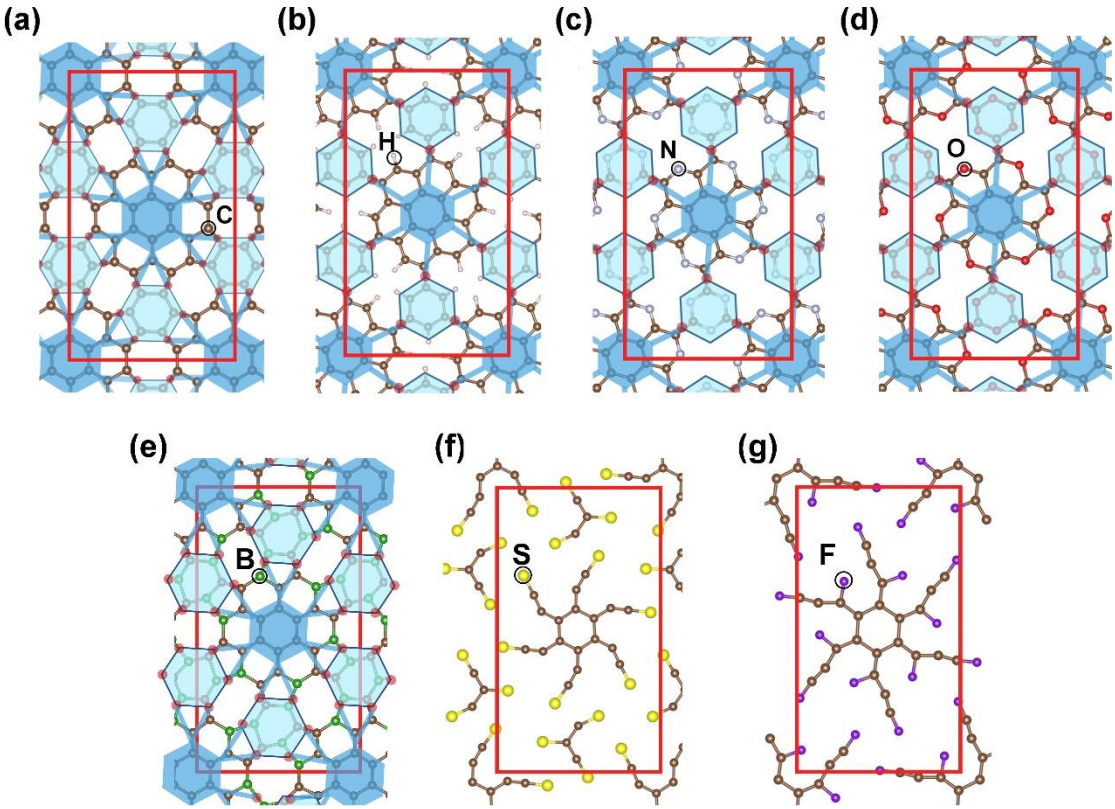

Figure S3. The equilibrium structures of pristine porous graphene (a) without and (b) with saturated Hydrogen atoms, (c) N-substituted, (d) O-substituted, (e) B-substituted, (f) S-substituted and (g) F-substituted porous graphene with corresponding kirigami assemblies.

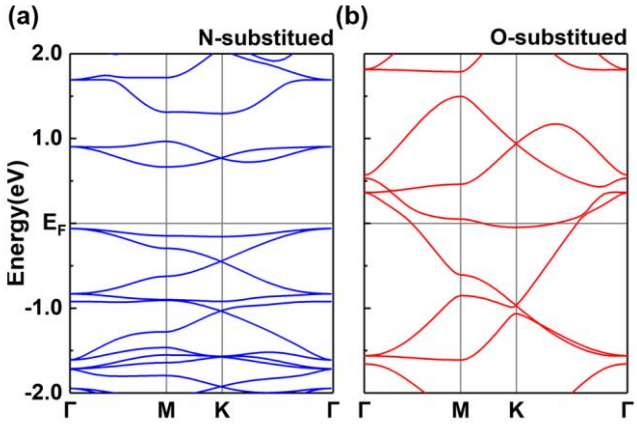

Figure S4. Band structures of (a) N-substituted and (b) O-substituted porous graphene.

The thermal dynamical stability of NPG was further studied by the *ab initio* molecular dynamical simulation and phonon dispersion of NPG. For a period of 10 ps in 500 K, shown in Fig. S5. The maximum energy fluctuation of NPG is 43 meV/atom, further confirming the superior dynamical stability. Indeed, the phonon dispersion of NPG free from imaginary frequency shown in Fig. S6 also illustrates the stability of NPG.

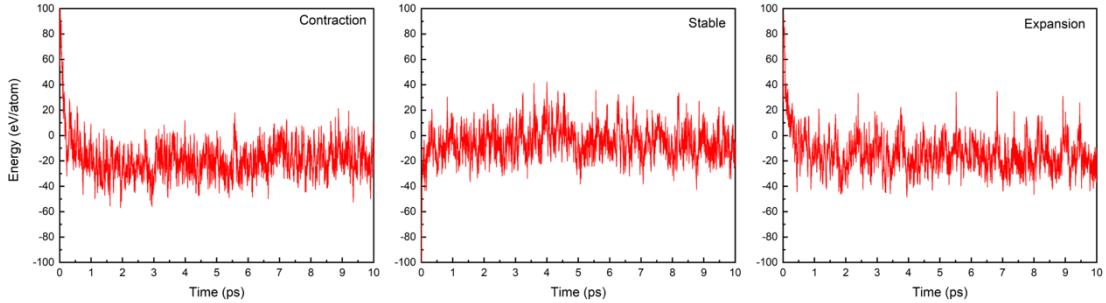

Figure S5. Potential energy per atom as a function of time in AIMD of NPG with time step as 3 fs for a period of 10 ps.

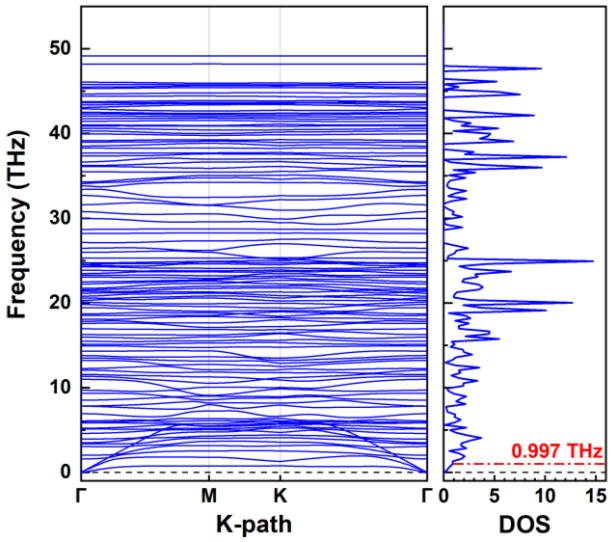

Figure S6. Phonon dispersion and density of states of NPG.

Besides, based on phonon dispersion and density of states of NPG. We can discuss the characteristic length and validate the effective medium concept of metamaterial about NPG. Since our NPG has a metal-insulator transition, heat is mainly carried by electrons for metals. For insulators, phonon dominates heat transport. Since the electron does not define the effective medium concept, we focus on the insulator state.

On the one hand, the NPG has a typical length of the unit cell (a=11.24 Å and b=19.48 Å). On the other hand, we add a figure of the phonon density of states of NPG material, shown below. Acoustic phonons mainly carry heat. We mark a prominent phonon mode in the dashed red line in the phonon density of states. It corresponds to the phonon frequency value of 0.997 THz. Here we consider uniform monolayer graphene as an effective medium that has a 22.1 km/s sound velocity of longitudinal acoustic (LA) phonon mode from the continuum approach [78]. As a metamaterial, the typical phonon has a wavelength, $\lambda = v/f$, where v is the sound velocity of LA phonon mode (effective medium concept) and f is the phonon frequency corresponding to the density of states. Therefore, the wavelength λ is 221.66 Å. This value is much larger than the typical length of the unit cell, indicating the validation of the effective medium concept and metamaterial in our paper.

Moreover, there are experimental methods to obtain NPG, such as liquid-liquid interfacial reaction [79,80], surface-assisted cyclodehydrogenation [81,82], chemical vapor deposition (CVD) [83], flux growth [84], and chemical synthesis [85,86,87] by monomers (triazine and N-doped coronene), shown in Fig. S7.

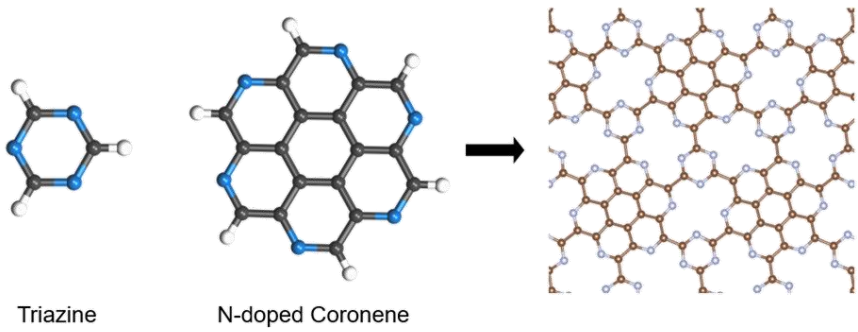

Figure S7. Potential experimental synthesis from Triazine and N-doped Coronene to NPG.

Guided by the *ab initio* calculation, we obtain the strain in the x and y directions during deformation with different θ. We define the reference lengths of x_0' and y_0'. We compare strain curves of NPG and corresponding theoretical kirigami assembly, shown in Fig. S8.

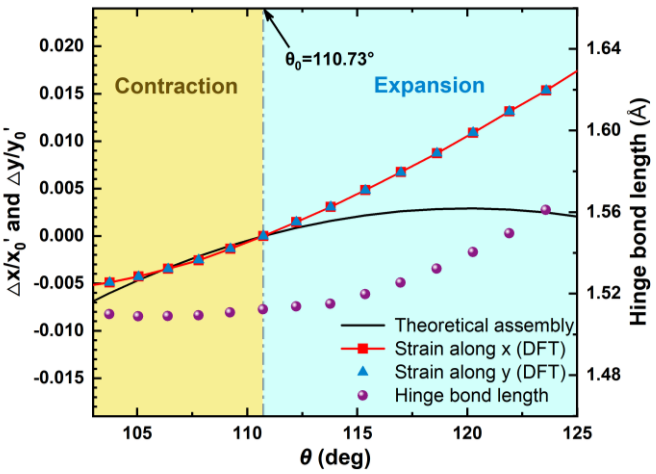

Figure S8. Strain curves along x and y directions and hinge bond lengths dependence of θ in NPG. The solid red line indicates the fitting strain curve of NPG, while the solid black line shows the strain curve of theoretical assembly. Light blue balls offer a change of hinge bond length.

The strain in the two directions of NPG is nearly equal, which means the Poisson's ratios of NPG are close to −1, similar to the Poisson's ratio of kirigami assembly. The strain curve of NPG matches the theoretical curve well in contraction, but deviates significantly in expansion. The difference between expansion and contraction in NPG is the increase in hinge bond length. However, the bond should be treated as a spring rather than a hinge. Based on this method, the corresponding models are shown in Fig. S9.

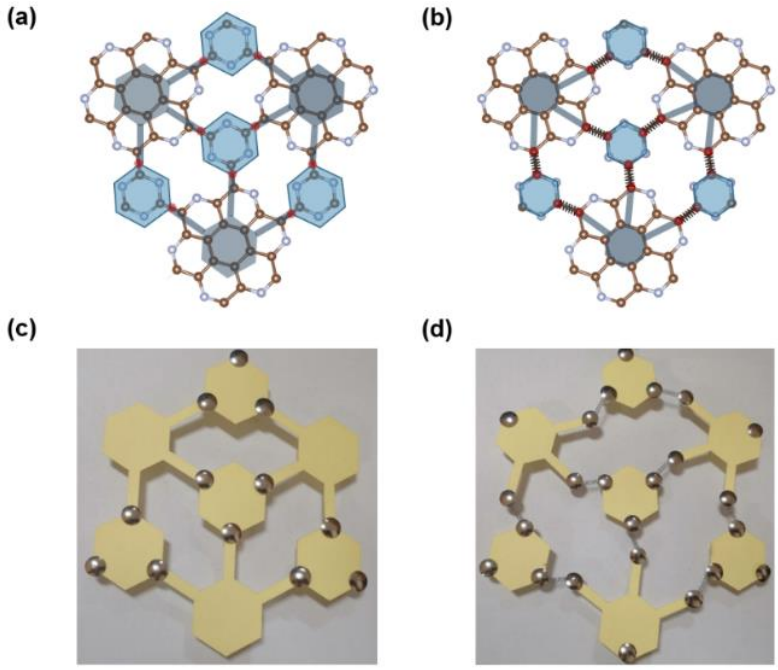

Figure S9. The corresponding assemblies and models of NPG when bonds are treated as hinges (a, c) or asymmetric springs (b, d), respectively.

According to the Lennard–Jones potential, the energy changes faster when the interatomic

distance decreases than increases. Thus, we suggest that the bond connecting different modules can be treated as an asymmetric spring. The bond is easier to extend than contract, so the folding-unfolding deformation dominates in contraction, while the extension of bonds dominates in expansion.

To support this explanation, we have collected the hinge bond length of different values of θ, shown in Fig. S8. The hinge bond length changes slightly in contraction while increasing drastically in expansion. It supports the "asymmetric spring effect" mentioned above, which is helpful for mapping from kirigami assemblies on microscale metamaterials in deformation behavior.

The lattice thermal transport properties were studied by non-equilibrium molecular dynamics (NEMD) shown in Fig. S10 and Fig. S11.

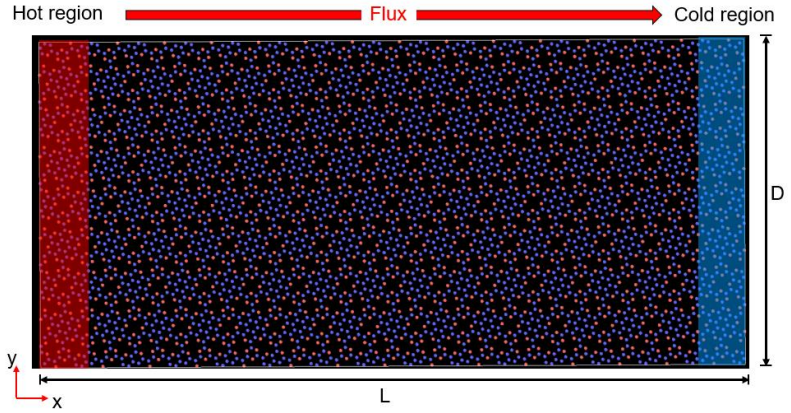

Figure S10. Schematic for NEMD of NPG, with temperatures in hot region (red) and cold region (blue) set as 320 K and 280 K, respectively.

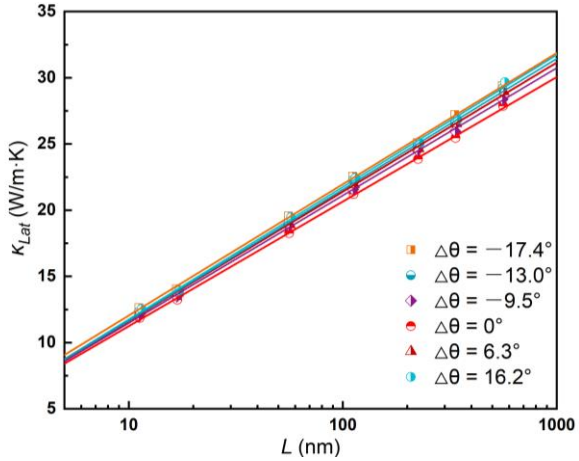

Figure S11. Lattice thermal conductivity as a function of length in NPG. Solid lines are logarithmic fitting of data with a function $\kappa_{lat} = \alpha \lg L$. α = 7.661, 7.574, 7.557, 7.498, 7.373, and 7.197 corresponds to $\Delta\theta = -17.4°$, $-13.0°$, $-9.5°$, 0°, 6.3°, and 16.2°, respectively.

Indeed, we shall see previous works find anomalous heat conduction of $\kappa_{lat} \propto \lg L$ (L is the sample length) in monolayer graphene [64, 65] and $\kappa_{lat} \propto L^{\alpha}$ with $0 < \alpha < 1$ in 1D lattice systems [66, 67]. Therefore, we study the length dependence of κ_{lat} shown in Fig. S11 which is quite

like graphene.

Indeed, the large number of atoms (72 atoms) in the unit cell of this metamaterial leads to an increase in the corresponding calculations as the number of cells increases. We built devices with different lengths, the unit cell was repeated 3, 4, 5, 6, 7, 8, 9, and 10 times in x direction, and the unit cells on two sides were treated as semi-infinite electrodes, while the center unit was regarded as a scattering region, shown in Fig. S12. The cutoff energy and k-point mesh were set to 20 Hartree and 100 × 1 × 1, and the bias voltage was set to 0.6 V.

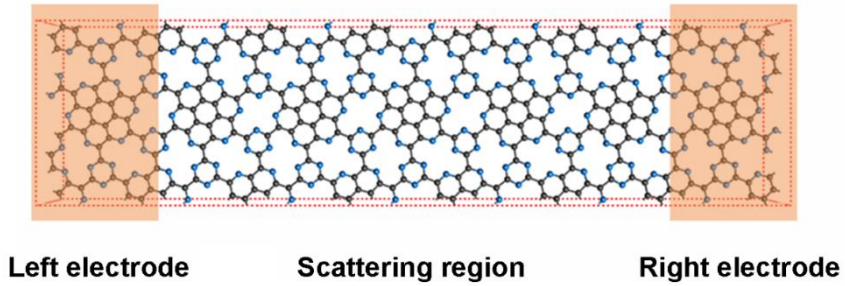

Figure S12. Schematic device for electronic transport property calculation based on NPG, with the potential bias set in two electrodes. Black and blue balls represent carbon and nitrogen atoms, respectively.

Based on the ATK package, the drain current is calculated and shown in Fig. S1. In this figure, the curve declines and converges after the scale of the device is larger than 7 unit cells, indicating that the scale of 7 unit cells in our manuscript can satisfy the convergence condition for electronic transport properties calculation. To balance the accuracy and amounts of calculation, we select the device of this scale to study the electronic transport properties of NPG devices.

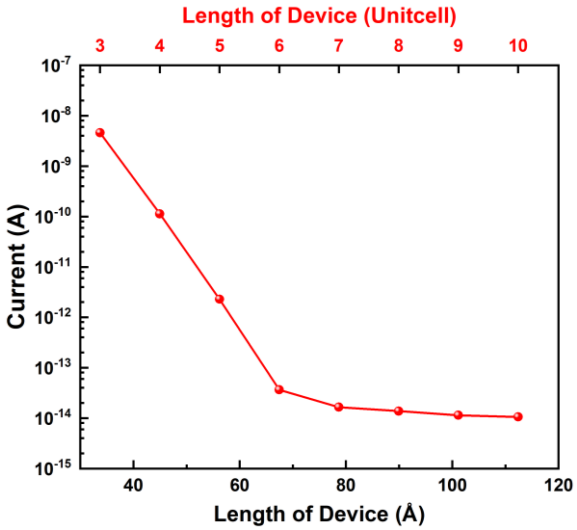

Figure S13 The current plot along with the NPG device's length. The bias voltage is 0.6 V. Note the scale of 7 unit cells can satisfy the convergent condition for calculating the electronic transport properties of the NPG device.

The electronic transport properties were studied by non-equilibrium molecular dynamics (NEMD). The electrical conductivities can be calculated based on the NPG device's current-voltage curves with different Δθ, shown in Fig. S14. The electrical conductivities of NPG with different doping carrier concentrations are obtained by setting the doping parameter in the calculation, shown in Fig. S15. The electronic thermal conductivity can be obtained according to the Wiedemann–Franz (WF) law, shown in Equation (5) of the main text. The results are shown in Fig. S16. Detailed data are shown in Table S1, Table S2, and Table S3.

In this part, we should discuss why the WF law is suit for calculating κ_{el} of NPG. The WF law holds only when the energy of each electron is conserved in each collision. Generally, there are four scattering mechanisms: (1) acoustic deformation potential scattering, (2) piezoelectric scattering, (3) polar optical phonon scattering, and (4) ionized impurity scattering. Except for (2) having an inelastic type, the other three are elastic scattering. Interestingly, a high-profile experimental paper [56], confirmed that the carriers in graphene exhibit the Fermi liquid paradigm, suggesting the satisfaction of the Wiedemann-Franz law. Besides, the paper also found the breakdown of the Wiedemann-Franz law in the thermally populated charge-neutral plasma in graphene, which is not the situation of NPG in our manuscript. Therefore, pure graphene holds the standard Sommerfeld value of Lorenz ratio, derived from Fermi liquid theory.

Moreover, the scattering between longitudinal-acoustic phonons and electrons can well-describe most materials, such as nonpolar crystals [57], carbon and organic nanomaterials [58], monolayer MoS_2 nanoribbons [59], anisotropic 2D SiS [60], and anisotropic 2D tellurene [61].

Since our NPG has no dangling bonds and never has a permanent dipole moment, it is a nonpolar crystal. According to the deformation potential theory from J. Bardeen and W. Shockley [57], the scattering mechanism in our NPG can be well described by the elastic acoustic deformation potential scattering. Consequently, the WF law holds in our NPG.

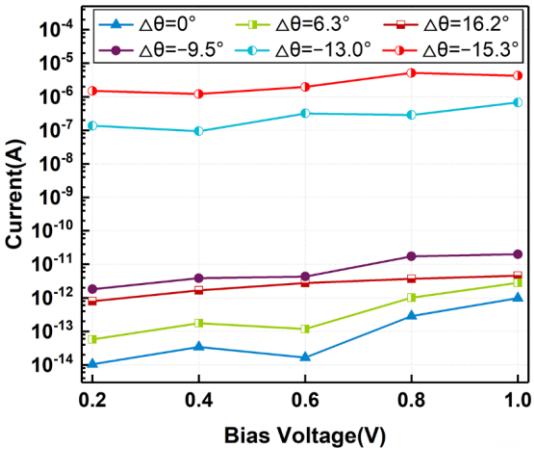

Figure S14. Current-voltage curves of NPG device with different Δθ.

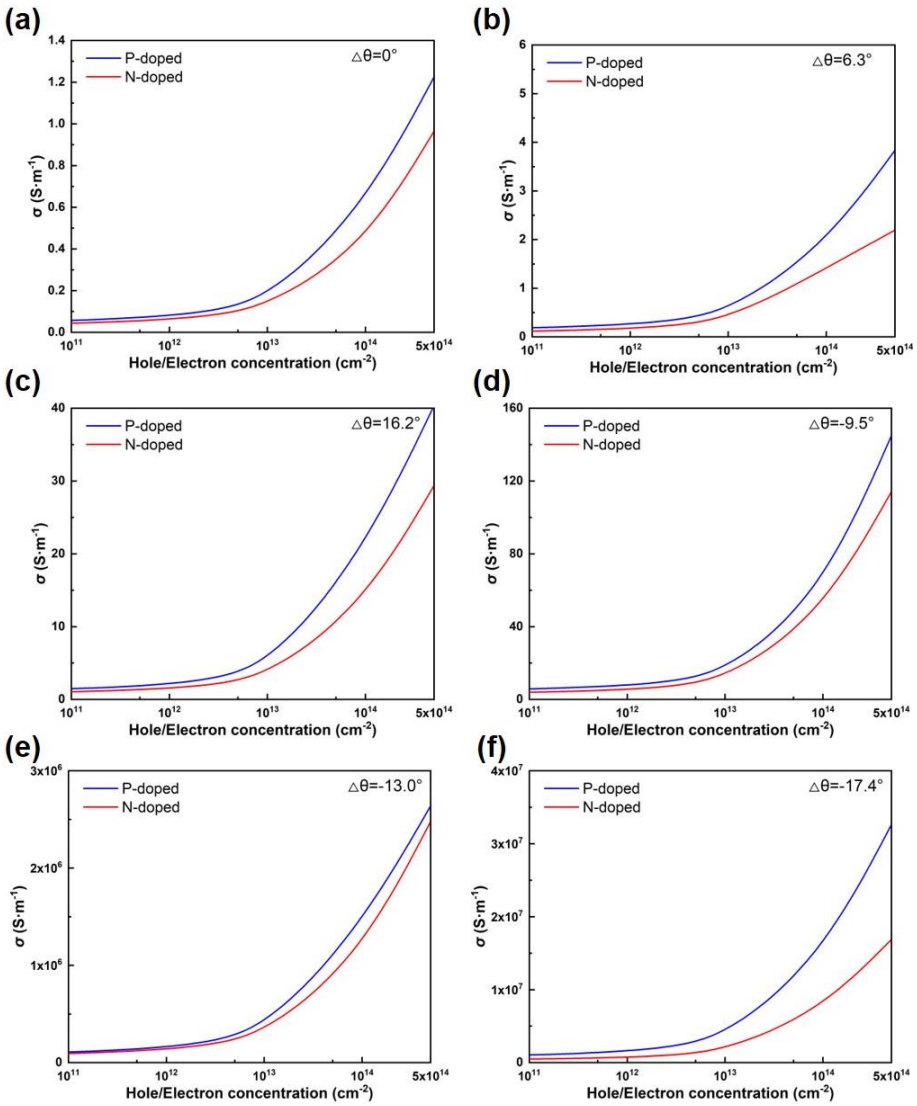

Figure S15. Electrical conductivities of NPG as a function of the hole and electron doping concentrations with (a) $\Delta\theta = 0°$, (b) $\Delta\theta = 6.3°$, (c) $\Delta\theta = 16.2°$, (d) $\Delta\theta = -9.5°$, (e) $\Delta\theta = -13.0°$, and (f) $\Delta\theta = -17.4°$, respectively.

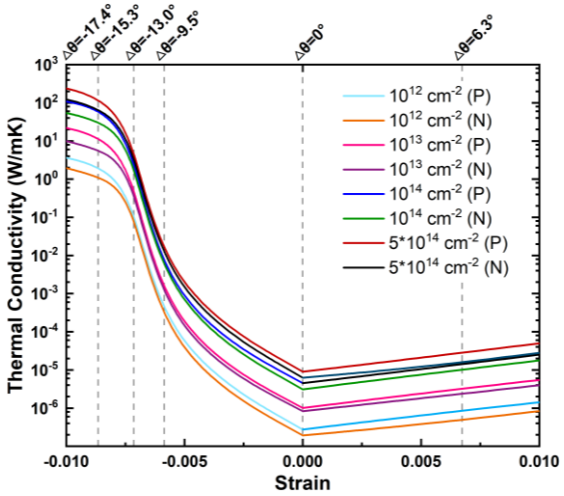

Figure S16. Electronic thermal conductivity of NPG as a function of strain in 300 K with different doping carrier types and concentrations.

Table S1 Current of NPG device with different Δθ and bias voltage. (unit: A)

Δθ	0°	6.3°	16.2°	-9.5°	-13.0°	-17.4°
0.2 V	1.05×10^{-14}	5.79×10^{-14}	7.85×10^{-13}	1.81×10^{-12}	1.36×10^{-7}	1.49×10^{-6}
0.4 V	3.43×10^{-14}	1.75×10^{-13}	1.67×10^{-12}	3.84×10^{-12}	9.36×10^{-8}	1.21×10^{-6}
0.6 V	1.65×10^{-14}	1.17×10^{-13}	2.76×10^{-12}	4.32×10^{-12}	3.17×10^{-7}	1.97×10^{-6}
0.8 V	2.86×10^{-13}	1.01×10^{-12}	3.70×10^{-12}	1.73×10^{-11}	2.85×10^{-7}	5.15×10^{-6}
1.0 V	9.76×10^{-13}	2.81×10^{-12}	4.58×10^{-12}	1.99×10^{-11}	6.75×10^{-7}	4.25×10^{-6}

Table S2 Electronic conductivities of NPG device for different hole and electron doping concentrations with different Δθ. (unit: S/m)

Doping concen-traition(cm^{-1})	Pristine	10^{12}	10^{13}	10^{14}	5×10^{14}
Δθ=0°					
Hole doping	9.09×10^{-4}	3.75×10^{-2}	0.137	0.614	1.23
Electron doping		2.62×10^{-2}	0.113	0.422	0.965
Δθ=6.3°					
Hole doping	5.96×10^{-3}	0.120	0.454	1.92	3.83
Electron doping		6.3×10^{-2}	0.325	1.42	2.19
Δθ=16.2°					
Hole doping	5.68×10^{-2}	0.647	2.69	13.4	29.4
Electron doping		0.908	3.69	20.8	40.4
Δθ=-9.5°					
Hole doping	0.166	4.35	12.4	59.6	1.45×10^{2}
Electron doping		2.74	9.08	47.9	1.14×10^{2}
Δθ=-13.0°					
Hole doping	5.13×10^{3}	5.85×10^{4}	2.94×10^{5}	1.42×10^{6}	2.64×10^{6}
Electron doping		5.16×10^{4}	2.53×10^{5}	1.13×10^{6}	2.48×10^{6}
Δθ=-17.4°					
Hole doping	5.35×10^{4}	4.96×10^{5}	3.00×10^{6}	1.48×10^{7}	3.26×10^{7}
Electron doping		2.65×10^{5}	1.35×10^{6}	7.41×10^{6}	1.69×10^{7}

Table S3 Electronic thermal conductivities (κ_{el}) of NPG device for different hole and electron doping concentrations with different Δθ. (unit: W/mK)

Doping concen-traition(cm^{-1})	Pristine	10^{12}	10^{13}	10^{14}	5×10^{14}
Δθ=0°					
Hole doping	6.66×10^{-9}	2.75×10^{-7}	1.01×10^{-6}	4.49×10^{-6}	8.97×10^{-6}
Electron doping		1.92×10^{-7}	8.30×10^{-7}	3.09×10^{-6}	6.25×10^{-6}
Δθ=6.3°					
Hole doping	4.38×10^{-8}	8.79×10^{-7}	3.33×10^{-6}	1.40×10^{-5}	2.81×10^{-5}
Electron doping		4.63×10^{-7}	2.38×10^{-6}	1.04×10^{-5}	1.43×10^{-5}
Δθ=16.2°					
Hole doping	5.84×10^{-7}	6.65×10^{-6}	2.70×10^{-5}	1.52×10^{-4}	2.95×10^{-4}
Electron doping		4.74×10^{-6}	1.97×10^{-5}	9.84×10^{-5}	1.94×10^{-4}
Δθ=-9.5°					
Hole doping	1.21×10^{-6}	3.18×10^{-5}	9.05×10^{-5}	4.37×10^{-4}	1.06×10^{-3}
Electron doping		2.00×10^{-5}	6.65×10^{-5}	3.51×10^{-4}	7.93×10^{-4}
Δθ=-13.0°					
Hole doping	3.75×10^{-3}	0.428	2.15	10.4	19,3
Electron doping		0.378	1.85	8.27	15.1
Δθ=-17.4°					
Hole doping	0.392	3.63	22.0	1.09×10^{2}	2.39×10^{2}
Electron doping		1.94	9.90	54.3	1.24×10^{2}

To evaluate the optical absorption ability, we studied the absorption spectra of NPG with different states, as shown in Fig. S16. The absorption spectra of materials are usually obtained from the dielectric function $\varepsilon(\omega) = \varepsilon_1(\omega) + i\varepsilon_2(\omega)$, from which the absorption coefficient can be calculated by the formula $\alpha(E) = (\sqrt{2}\omega/c)\{[(\varepsilon_1^2 + \varepsilon_2^2)^{1/2} - \varepsilon_1]\}^{1/2}$. Around infrared, which is noted in Fig. S16(d), a new absorption peak emerges in contraction with $\Delta\theta = -17.4°$, which is in accordance with the variation of the band gap shown in the main text. This new absorption peak is owing to MIT, which results in the absorption of photons with low energy in NPG.

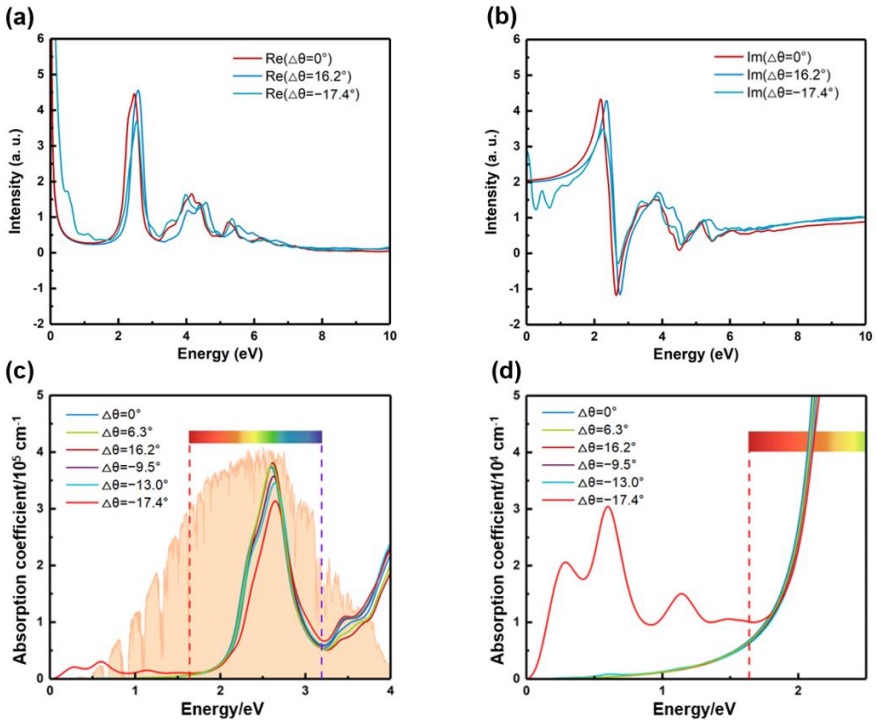

Figure S16. Relationships between (a) the real part and (b) the imaginary part of the dielectric function and energy of electromagnetic waves for different states. (c) Optical absorption spectra with different NPG and solar radiation spectrum (orange areas). (d) The zoom feature of optical absorption spectra in the infrared area, in which absorption peak occurs in contraction. The solar radiation spectrum is taken from the NREL website (https://www.nrel.gov/grid/solar-resource/spectra-am1.5.html).

We also calculated the thermal expansion of NPG shown in Fig. S17. The lattice constant decreases with increasing temperature, indicating a negative thermal expansion (NTE) of NPG [76]. We obtained NTE of NPG ranging from -6×10^{-6} K^{-1} to -1×10^{-6} K^{-1} as a function of temperature. Single-layer graphene also has the same order of NTE with -8×10^{-6} K^{-1} measured by Raman spectroscopy [77].

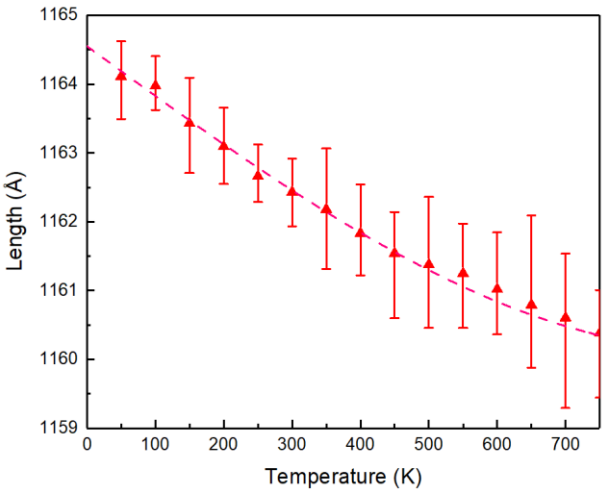

Figure S17. Relationship between temperature and length of NPG in the MD simulation.

To verify the stability and practicability, we study the strain energy of NPG presented in Fig. S18. What's more, we calculate the formation energy for NPG relative to graphene can be calculated as, $E = E_{NPG} - E_{graphene}$. Where, E_{NPG} is the total energy of the NPG (including 24 Nitrogen atoms and 48 Carbon atoms), and $E_{graphene}$ is the total energy of graphene (including 72 Carbon atoms), respectively. The calculated formation energy was found to be 21.604 eV for the NPG of 1 unit cell relative to graphene structures and 0.90 eV for each Carbon atom, indicating the thermodynamic stability of NPG.

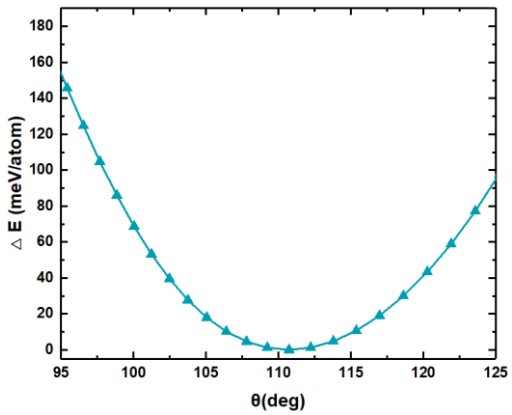

Figure S18. Strain energy per atom in NPG as a function of θ.

Video 1: Folding-unfolding deformation of kirigami assembly.

Video 2: Folding-unfolding deformation of NPG.

[48] L. Tsetseris, B. Wang, and S. T. Pantelides, Phys. Rev. B **89**, 035411 (2014).

[49] P. E. Blöchl, Phys. Rev. B **50**, 17953 (1994).

[50] G. Kresse and D. Joubert, Phys. Rev. B **59**, 1758 (1999).

[51] J. P. Perdew, K. Burke, and M. Ernzerhof, Phys. Rev. Lett. **77**, 3865 (1996).

[52] G. Kresse and J. Furthmüller, Comput. Mater. Sci. **6**, 15 (1996).

[53] G. Kresse and J. Furthmüller, Phys. Rev. B **54**, 11169 (1996).

[54] H. J. Monkhorst and J. D. Pack, Phys. Rev. B **13**, 5188 (1976).

[56] J. Crossno, J. K. Shi, K. Wang, X. Liu, A. Harzheim, A. Lucas, S. Sachdev, P. Kim, T. Taniguchi, and K. Watanabe, *Science* **351**, 1058 (2016).

[57] J. Bardeen and W. Shockley, *Phys. Rev. B* **80**, 72 (1950).

[58] J. Xi, M. Long, L. Tang, D. Wang, and Z. Shuai, *Nanoscale* **4**, 4348 (2012).

[59] Y. Cai, G. Zhang, and Y. W. Zhang, *J. Am. Chem. Soc.* **136**, 6269 (2014).

[60] J. H. Yang, Y. Zhang, W. J. Yin, X. Gong, B. I. Yakobson, and S. H. Wei, *Nano Lett.* **16**, 1110 (2016).

[61] Z. Zhu, X. Cai, S. Yi, J. Chen, Y. Dai, C. Niu, Z. Guo, M. Xie, F. Liu, and J.-H. Cho, *Phys. Rev. Lett.* **119**, 106101 (2017).

[62] S. Plimpton, *J. Comput. Phys.* **117**, 1 (1995).

[63] A. Kınac ı, J. B. Haskins, C. Sevik, and T. Çağ ın, *Phys. Rev. B* **86**, 115410 (2012).

[64] X. Xu, L. F. Pereira, Y. Wang, J. Wu, K. Zhang, X. Zhao, S. Bae, C. T. Bui, R. Xie, J. T. Thong, B. H. Hong, K. P. Loh, D.Donadio, B. Li, and B.Ozyilmaz, *Nat.Commun.* **5,** 3689 (2014).

[65] H. Wang, S. Hu, K. Takahashi, X. Zhang, H. Takamatsu, and J. Chen, *Nat. Commun.* **8,** 15843 (2017).

[66] S. Lepri, R. Livi, and A. Politi, *Phys. Rev. Lett.* **78,** 1896 (1997).

[67] Z. Gao, N. Li, and B. Li, *Phys. Rev. E* **93,** 022102 (2016).

[73] M. Brandbyge, J.-L. Mozos, P. Ordejón, J. Taylor, and K. Stokbro, Phys. Rev. B **65**, 165401 (2002).

[74] S. Smidstrup, T. Markussen, P. Vancraeyveld, J. Wellen-dor□, J. Schneider, T. Gunst, B. Verstichel, D. Stradi, P. A. Khomyakov, U. G. Vej-Hansen, M.-E. Lee, S. T. Chill, F. Rasmussen, G. Penazzi, F. Corsetti, A. Ojan-per¨a, K. Jensen, M. L. N. Palsgaard, U. Martinez, A. Blom, M. Brandbyge, and K. Stokbro, J. Phys.: Condens. Matter. **32**, 015901 (2019).

[75] S. Datta, Phys. Today **49**, 70 (1996).

[76] G. Liu, Z. Gao, and J. Ren, Phys. Rev. B **99**, 195436 (2019).

[77] D. Yoon, Y.-W. Son, and H. Cheong, Nano Lett. **11**, 3227 (2011).

[78] D. Liu, A. G. Every, and D. Tománek, *Phys. Rev. B* **94**, 165432 (2016).

[79] T. Kambe, R. Sakamoto, K. Hoshiko, K. Takada, M. Miy-achi, J.-H. Ryu, S. Sasaki, J. Kim, K. Nakazato, M. Takata, and H. Nishihara, J. Am. Chem. Soc. **135**, 2462 (2013).

[80] R. Sakamoto, K. Takada, T. Pal, H. Maeda, T. Kambe, and H. Nishihara, Chem. Commun. **53**, 5781 (2017).

[81] M. Treier, C. A. Pignedoli, T. Laino, R. Rieger, K. Müllen, D. Passerone, and R. Fasel, Nat.

Chem. **3**, 61 (2011).

[82] C. Moreno, M. Vilas-Varela, B. Kretz, A. Garcia-Lekue, M. V. Costache, M. Paradinas, M. Panighel, G. Ceballos, S. O. Valenzuela, D. Peña, and A. Mugarza, Science **360**, 199 (2018).

[83] H. Sugimoto, M. Fujii, and K. Imakita, RSC Adv. **5**, 8427 (2015).

[84] S. Liu, R. He, L. Xue, J. Li, B. Liu, and J. H. Edgar, Chem. Mater. **30**, 6222 (2018).

[85]M. Bieri, M. Treier, J. Cai, K. Aït-Mansour, P. Ru□eux, O. Gröning, P. Gröning, M. Kastler, R. Rieger, X. Feng, K. Müllen, and R. Fasel, Chem. Commun. **45**, 6919 (2009).

[86] L. F. Villalobos, M. T. Vahdat, M. Dakhchoune, Z. Nadizadeh, M. Mensi, E. Oveisi, D. Campi, N. Marzari, and K. V. Agrawal, Sci. Adv. **6**, eaay9851 (2020).

[87] Q. Tan, H. Chen, H. Xia, B. Liu, and B. Xu, Chem. Commun. **52**, 537 (2016).